

Quantum Optics Experiments as the means to study Fundamental Quantum Mechanics*

Mahid Anjum

*Many thanks to
Bilal Hyder [3],
Dr Muhammad Sabieh Anwar &
Physlab.

Contents

1	Components & software used	3
2	Spontaneous parametric down-conversion	6
2.1	Theoretical background	6
2.2	Experiment & results	8
3	Experiments exploring entanglement & nonlocality	13
3.1	Freedman's test of local realism	15
3.1.1	Aligning the four detector arrangement	17
3.1.2	Generating the state $ \Phi^+\rangle$	19
3.1.3	Experiment & results	21
3.2	CHSH test of local realism	21
3.2.1	Experiment & results	22
3.3	Hardy's test of local realism	24
3.3.1	Generating the state $ \Psi\rangle$	25
3.3.2	Experiment & results	25
4	Quantum state tomography	27
4.1	Theoretical background	27
4.1.1	The density matrix formalism	27
4.1.2	Two-qubit states & theory governing two-qubit QST	28
4.1.3	Density matrix characterization quantities	30
4.2	Experiment & results	31
4.2.1	$ HH\rangle$ state	32
4.2.2	$ VV\rangle$ state	34
4.2.3	$ \Phi^+\rangle$ state	36
4.2.4	$ \Phi^+\rangle_\phi$ state	38
	Bibliography	40

Components & software used

‘Every tool carries with it the spirit by which it has been created.’

Werner Heisenberg

- Pump laser: A 405 nm violet laser was used as the pump laser. It is collimated & puts out light in the vertically polarized state $|V\rangle$.

Symbol:



- BBO stack: Two BBO crystals stacked in the middle of a disk mounted on a kinematic mount. This stack was used to carry out SPDC (refer section 2.1 for further details).

Symbol:



- Photon collectors: These collect the incident light and carry the collected light to the single photon counting module using an optical fiber.
- SPCM - Single photon counting module: Avalanche photo-diodes. These generate an electric pulse each time a photon is received. A photon collector & the SPCM connected to it will collectively be referred as a ‘detector’.

Symbol of a detector:



- HWP - Half wave plate: An optical component which rotates linearly polarized light.

Symbol:



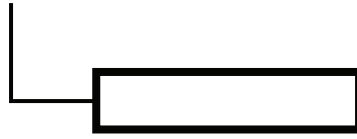
- QWP - Quarter wave plate: An optical component which converts linearly polarized light to circularly polarized light.

Symbol:



- Back propagation/alignment laser: 633 nm laser(s) for back-propagation alignment.

Symbol:



- Polarizing beam splitter: An optical component which splits incident light based on polarization. The PBS used in our experiments transmits vertically polarized photons $|V\rangle$ and reflects horizontally polarized photons $|H\rangle$.

Symbol:



- Motorized rotation stage and controller: Motorized stage for rotation of optical components. The controller can be tweaked using the software package provided.
- FPGA: In the FPGA a coincidence counting unit (CCU) has been implemented. Each time a pulse is produced by an SPCM, it is carried to the FPGA via BNC cables.

- Counting software:

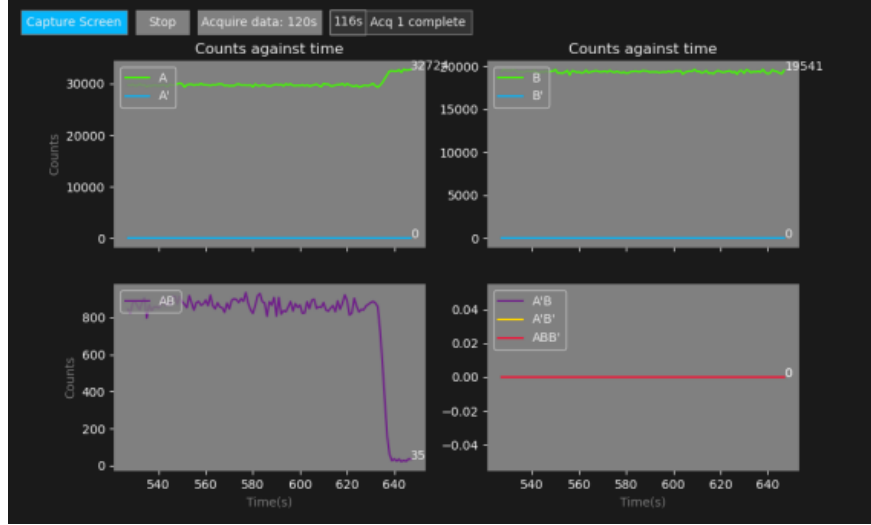


Figure 1.1: A screenshot of the counting GUI. Both single detector counts A , A' , B , B' & coincidence counts (detecting two or more photons simultaneously at different detectors) AB , $A'B$, $A'B'$, ABB' are displayed in real time.

Receives data from the FPGA and projects it in real-time onto an interactive GUI developed by B. Hyder [3].

- Quartz plate: A birefringent quartz plate used to control the phase ϕ between two polarizations of the incident light beam.

Symbol:



- Polarizer: An optical component that only lets light of a specific polarization pass through.

Spontaneous parametric down-conversion

Allow me to express now, once and for all, my deep respect for the work of the experimenter and for his fight to wring significant facts from an inflexible Nature . . . [which] says so distinctly No and so indistinctly Yes to our theories'

Hermann Weyl

To experimentally study the quantum nature of light, we need a quantum source of light, a source which can produce single photons. One physical phenomenon with which single photons can be produced is *Spontaneous Parametric Down-Conversion (SPDC)*. SPDC, albeit a very inefficient process [1], forms the bedrock of many experiments probing quantum mechanics.

Firstly I shed some light on the theory of this crucial phenomenon and then cover the experimental method followed to study this phenomenon in the laboratory. It is essential to highlight that this experiment was a rerun aiming to reproduce the results obtained in the book 'Quantum Mechanics in the Single Photon Laboratory' [2].

2.1 Theoretical background

In SPDC, an incident pump photon is converted into two *daughter* photons, namely 'signal' and 'idler' photons. Each daughter photon has frequency and energy half that of the pump photon. For this reason the daughter photons are dubbed the 'down-converted' photons. The process is illustrated in figure 2.1.

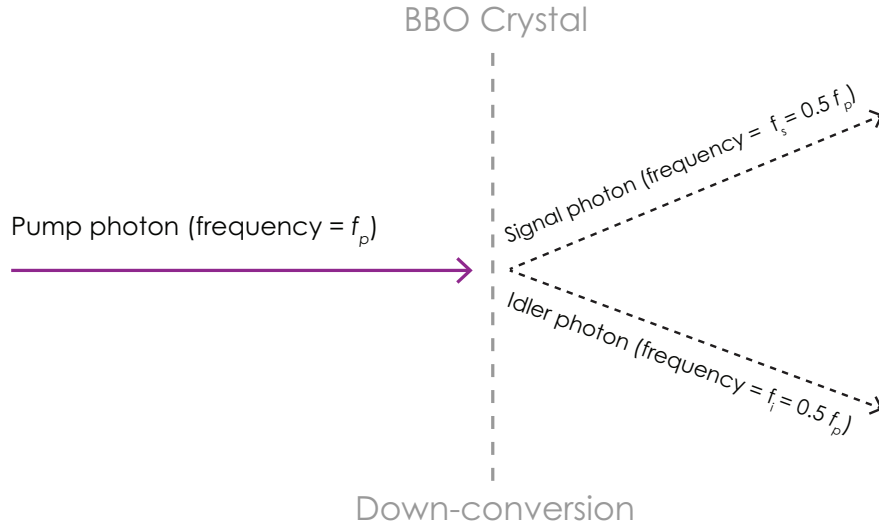


Figure 2.1: An incident pump photon is down-converted into two daughter photons. Each down-converted photon has a frequency half that of the pump photon. The medium used to carry out down-conversion is a BBO crystal.

The occurrence of SPDC is contingent upon a particular polarization of the pump photon i.e. only pump photons having a particular polarization are down-converted. This suggests a phase relationship exists between the pump beam and the down-converted beams. Furthermore, the

down-converted photons are always produced in pairs; this quirk of SPDC comes in handy as detecting one daughter photon would imply the presence of the other daughter photon.

In our experiment, a stack of two BBO crystals was used to carry out SPDC. Each crystal was cut out to carry out Type-I SPDC, meaning that both the down-converted photons would have a polarization orthogonal to that of the pump photon. Both crystals were stacked at 90° to each other. This stacking arrangement would allow one of the BBO crystals to down-convert vertically polarized photons $|V\rangle$ and the other crystal to down-convert horizontally polarized photons $|H\rangle$. The action of the BBO on the polarization of the pump photon is shown below,

$$\begin{aligned} |V\rangle &\xrightarrow{BBO} |HH\rangle, \\ |H\rangle &\xrightarrow{BBO} |VV\rangle. \end{aligned}$$

Here it down-converts one vertically polarized pump photon $|V\rangle$ into a pair of horizontally polarized down-converted photons $|HH\rangle$ & vice versa.

Theoretically, if one of the BBO crystals is misaligned, i.e. the relative angle between the crystals is no more 90° , then depending on which crystal is misaligned, either the vertically polarized pump photon $|V\rangle$ or the horizontally polarized pump photon $|H\rangle$ would no longer be catered. This would imply a decrease in the number of down-converted photons detected.

In practice, a half-wave plate (HWP) can rotate the linear polarization of an incident beam. At certain θ (angle between the polarization of the incident beam and the optical axis of the HWP) the HWP can change the incident photon in the vertically polarized state $|V\rangle$ to a photon in the horizontally polarized state $|H\rangle$ and vice versa. This means if a vertically polarized beam $|V\rangle$ is incident onto a HWP & the HWP is made to rotate over a range of θ , for certain θ it would change the polarization from $|V\rangle \rightarrow |H\rangle$. If this resultant beam is perpetually made incident onto a hypothetically misaligned BBO crystal which does not cater $|H\rangle$ while the HWP is rotating, then the horizontally polarized photons $|H\rangle$ would not be down-converted. This implies for some orientations of the HWP one would expect to see a dip in the number of down-converted photons detected for a misaligned crystal as mentioned earlier. Following similar arguments, it can be deduced that a hypothetically perfectly aligned BBO stack would be able to down-convert both the $|H\rangle$ and $|V\rangle$ polarizations of the pump photons. Hence no dips would be expected in the single-photon counts for an aligned BBO stack. The theoretical predictions put forth by these arguments are depicted in figure 2.2.

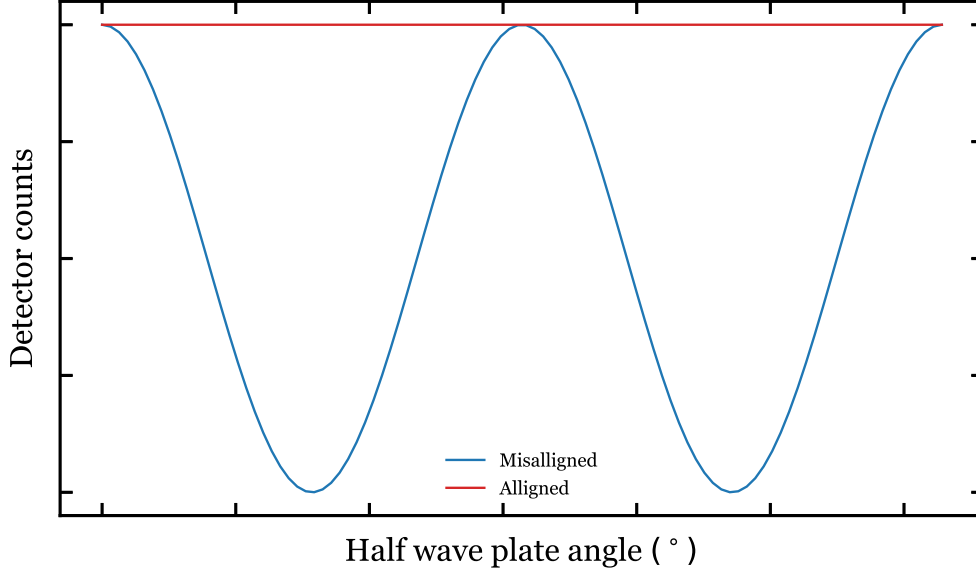


Figure 2.2: Expected relation between the number of down-converted photons detected (detector counts) & the orientation of the HWP. Both the aligned & misaligned cases for the BBO stack are shown.

2.2 Experiment & results

The first part of the setup was to ensure that the pump beam was aligned correctly and had a constant height at every point above the optical table. To accomplish this, the pump beam was reflected off two adjustable mirrors, this ensured there was no tilt present in the beam. The beam's constant height above the optical table was confirmed by placing an alignment ruler at different points in the beam's path and ensuring that at each point the beam coincided with the same marking on the ruler. Once the pump beam had been aligned, it was used as a reference to align the other components which were to be placed.

The BBO crystals used in the experiment were chosen such that both the down-converted daughter beams made an angle of 3° relative to the pump beam. These down-converted photons had a wavelength of 810 nm (twice the wavelength of the pump beam). Since this λ lies outside the visible part of the electromagnetic spectrum, it's quite challenging to align detectors A & B because the down-converted beams are invisible to the naked eye and cannot be used as a reference. To overcome this hindrance, the method of back propagation was utilized. Before back propagation could be implemented, the single photon detectors A & B had to be placed at roughly 3° relative to the pump beam. The distance between the midpoint of the detectors & the BBO crystals was chosen to be 48" in our setup (note that the choice of this distance lies completely with the experimenter). Exploiting the geometrical arrangement of the setup shown in figure 2.3, the expected distance between both the detectors A & B was estimated using simple trigonometry,

$$\begin{aligned} \text{Estimated distance} &= 2 \cdot (48'' \tan 3^\circ), \\ &\approx 5.03'' \approx 12.8 \text{ cm}. \end{aligned}$$

Both detectors A & B were then placed with separation between them equal to the estimated

distance.

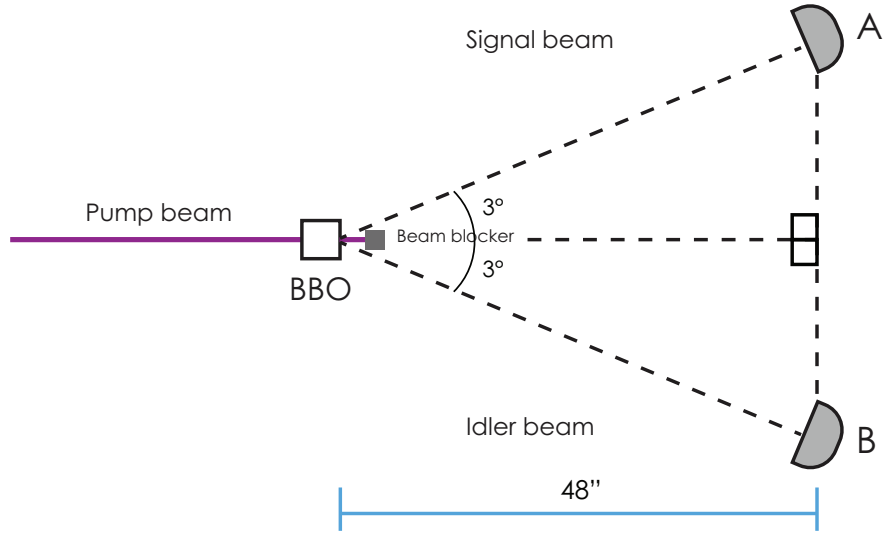


Figure 2.3: Geometrical arrangement before the back propagation method was utilized.

The pump laser was turned off before initiating the back propagation alignment procedure. Now a back propagation laser of wavelength 633 nm was connected to the photon collector which formed one half of detector A. The back propagation laser was shone backwards toward the BBO crystals & the knobs of the kinematic mount holding the collector were tweaked until the alignment laser was directly incident onto the centre of the BBO crystals. Using the alignment ruler it was ensured that the back propagation laser, on its path back to the BBO crystals, had a constant height above the optical table. At this point, detector A had been roughly aligned. Similar procedure was followed for coarsely aligning detector B. Once both the detectors had been coarsely aligned separately, one alignment laser was connected to each detector and shone backwards. The knobs of the holders were tweaked further until both the alignment lasers coincided at the center of the BBO crystal stack. This last step shown in figure 2.4 improved the alignment of the detectors.

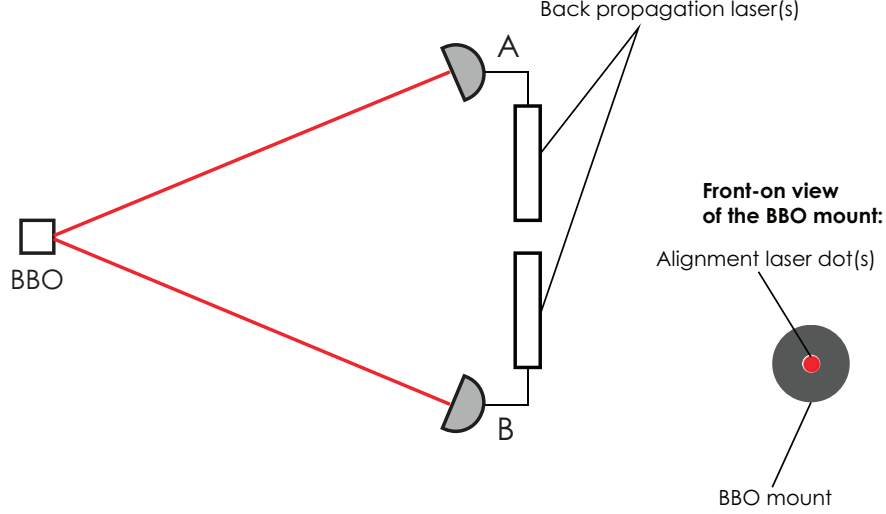


Figure 2.4: Two back propagation lasers shone backwards towards the BBO stack to fine-tune the coarse alignment of detectors A & B.

The alignment lasers were disconnected and the SPCMs were connected back to the photon collectors. At this point, rough alignment of the detectors was complete.

The pump laser was turned on and made incident on the not yet aligned BBO crystals. With both the detectors roughly aligned and their outputs connected to the PC, the individual counts A, B, & the coincidence counts AB were being displayed on the counting software in real-time. It was observed that several counts were being registered on the counting software for both detectors A & B. This was because both the detectors had been coarsely aligned previously. To carry out fine alignment of the detectors the tilt of the detectors was tweaked using the rotating knobs of the mounts until both the individual & coincidence counts were maximized. The experimental arrangement hitherto is shown in figure 2.5.

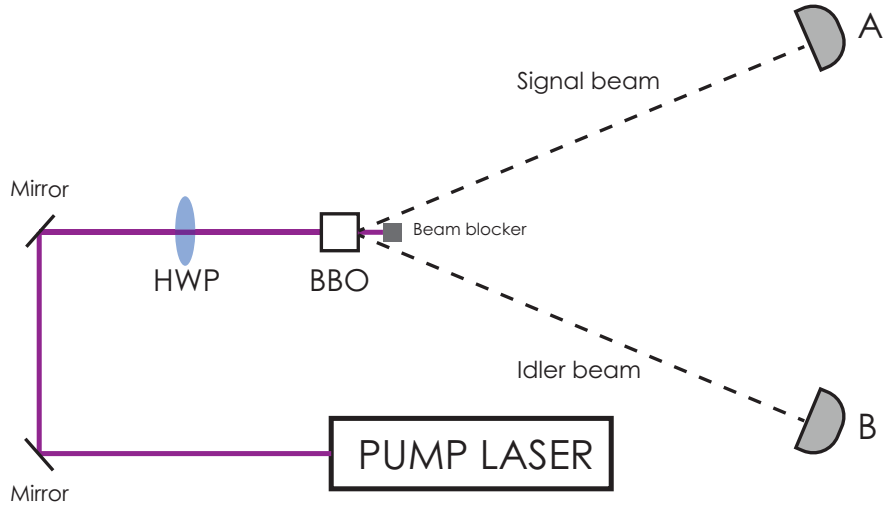
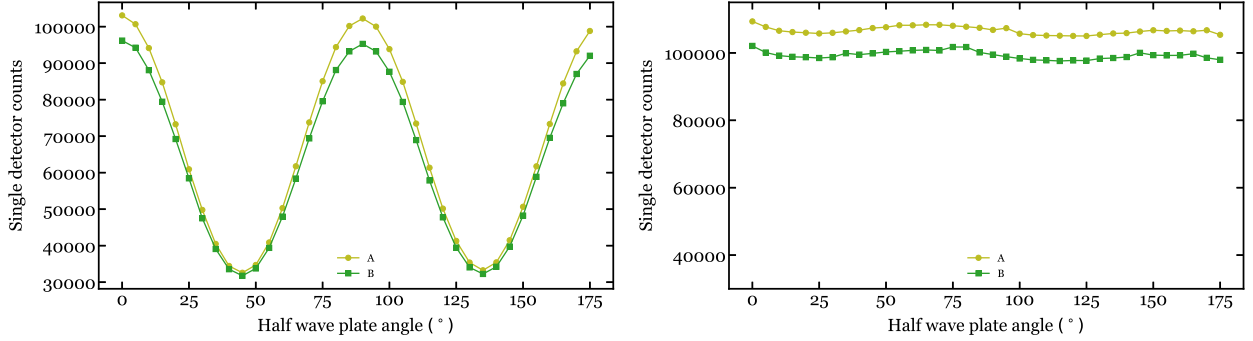


Figure 2.5: Experimental arrangement with both the detectors aligned. This setup was used to study SPDC and align the BBO crystal stack.

Up until now the polarization of the pump beam had not been altered by the HWP and the

state input to the BBO was $|V\rangle$; the same state output by the pump laser. This implies that the down-conversion undertaken by the misaligned BBO stack until now had been of the $|V\rangle$ state only. This was brought to light once the HWP was oriented at angles ranging from $0^\circ - 180^\circ$ in steps of 5° and the corresponding counts at each HWP orientation collected. At each angle in the aforementioned mentioned range, a 10s data acquisition was carried out utilizing the counting software. Results obtained are shown in figure 2.6a. On inspecting figure 2.6a, it can be deduced that the dips arise when the HWP is at 45° & 135° affirming that the BBO crystal responsible for carrying out down-conversion of $|H\rangle$ photons is misaligned.



(a) BBO crystal responsible for down-converting $|H\rangle$ photons misaligned.

(b) Both BBO crystals aligned.

Figure 2.6: Variation of the single detector counts for misaligned (figure 2.6a) & aligned (figure 2.6b) BBO crystals. The background counts for both the detectors have been subtracted from the raw counts to obtain the true counts which are displayed in the plot(s) above. The data cleaning model used for the single detector counts was suggested in [4].

To align the misaligned BBO crystal responsible for down-converting the $|H\rangle$ input state, we input the $|H\rangle$ state to the BBO by setting the pump beam HWP at 45° and then tune the BBO tilt using the knobs on the kinematic mount until the coincidence counts are maximized. Only one knob of the rotating mount was tuned since the crystal responsible for down-converting $|V\rangle$ input state was already aligned. After the alignment was complete, the HWP was rotated again over the aforementioned angular range to ensure both the BBO crystals were optimally aligned. As predicted in figure 2.2, one would expect minimal change in the counts if both the BBO crystals are properly aligned & indeed this is what we observe in figure 2.6b.

Raw data collected for the coincidence counts AB had to be cleaned as well before the true coincidence counts could be plotted. To determine the true coincidence counts, equation 2.1 devised in [4] was used.

$$N_{AB}^{true} = N_{AB}^{raw} - N_{AB}^{acc}, \quad (2.1)$$

$$\therefore N_{AB}^{acc} = N_A N_B \delta t,$$

where N_{AB}^{true} are the true coincidence counts, N_{AB}^{raw} are the raw coincidence counts, N_{AB}^{acc} are the accidental coincidence counts, N_A & N_B are the single detector counts, and δt is the time window for the pulses to get registered in our FPGA, in our case $\delta t = 20$ ns. Figure 2.7 shows the raw and true coincidence counts for both the aligned and misaligned BBO stack.

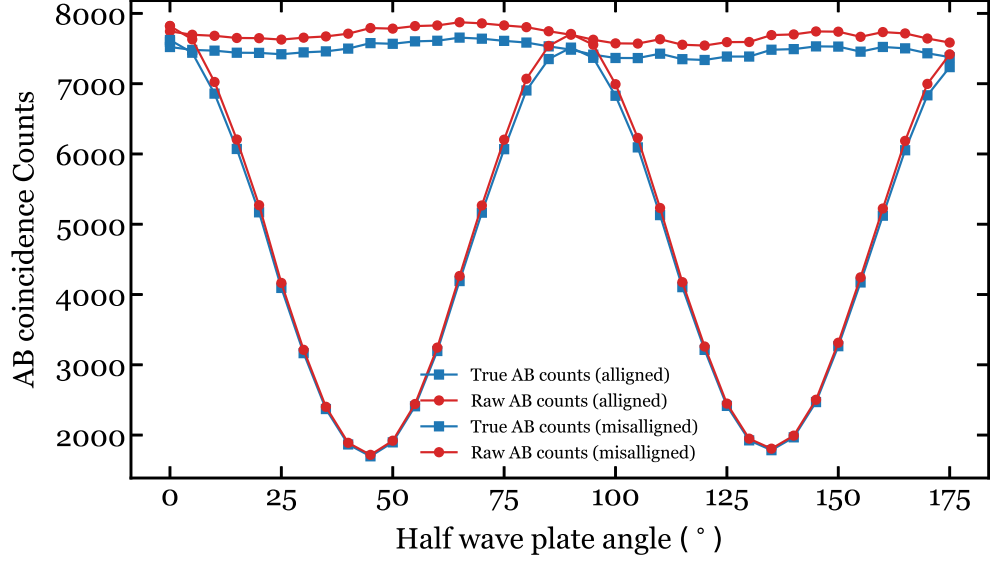


Figure 2.7: Plot comparing the raw & true coincidence counts for the misaligned & aligned BBO stack. By inspecting the plots it can be deduced that the accidental coincidence counts N_{AB}^{acc} are of the order $\sim 10^2$.

We are particularly interested in the coincidence counts since these counts show the presence of ‘genuine’ single photons. This is due to the fact that down-converted photons are always produced in pairs, hence detecting two photons simultaneously (within 20 ns) at two different detectors implies that both the detected photons were produced due to down-conversion of the same pump photon. Now that the BBO stack is optimally aligned, SPDC can be utilized as a true single photon source for further experiments to be carried out.

Experiments exploring entanglement & nonlocality

'spooky action at a distance'

Albert Einstein

While studying SPDC we studied single photon systems i.e. we looked at both the down-converted beams separately and were not interested in finding out any correlation between the polarizations of the two beams. In the upcoming experiments we consider two-photons systems i.e. we study the down-converted beams jointly, exploring the seemingly bizarre phenomenons of quantum entanglement and nonlocality. Quantum entanglement has no parallel in classical physics and is accredited for the disparity between classical & quantum physics. Local realism, obeyed by all classical systems, implies that any measurement that can be performed on one photon of an entangled photon pair cannot affect the state of the other member of the pair. Through the experiments performed in this chapter we reaffirm that quantum entanglement violates local realism and is indeed non-local in its nature.

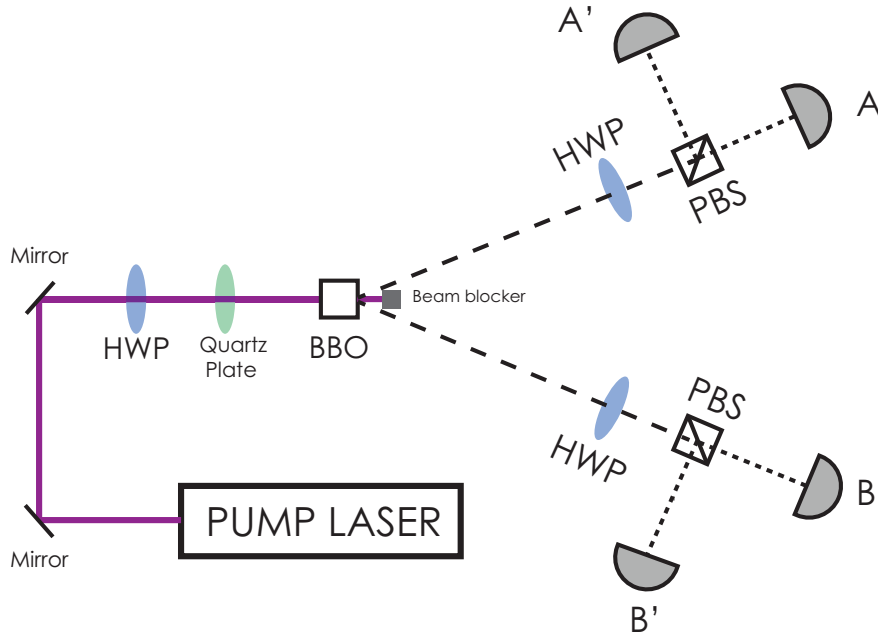


Figure 3.1: A four-detector arrangement for the entanglement experiments/tests. This arrangement was used to generate the states required in the local realism tests conducted. Channel A comprises of the signal beam, detectors A & A' and a set of HWP & PBS, whereas channel B comprises of the idler beam, detectors B & B' and a set of HWP & PBS. The combination of HWP + PBS in both channels enacts the working of a polarizer.

A general two-photon state in the $\{|H\rangle, |V\rangle\}$ basis is written as follows,

$$|\psi\rangle = A |H\rangle_A |H\rangle_B + B e^{i\phi} |V\rangle_A |V\rangle_B, \quad (3.1)$$

$$|\psi\rangle = A |HH\rangle + B e^{i\phi} |VV\rangle, \quad (3.2)$$

here the subscripts A & B essentially label the two different channels the down-converted photons could traverse through. These subscripts can be used to represent the *signal* and *idler* channels in the SPDC arrangement. The transition from equation 3.1 to equation 3.2 is based on the postulate that the first letter inside each ket in equation 3.2 is the polarization of the channel A photon and the second letter is the polarization of the channel B photon, respectively. Two or more particles are said to be entangled if their individual states cannot be written independently from the *shared* state of the particles. Utilizing equation 3.2 we can generate states that are linear combinations of the states $|HH\rangle$ & $|VV\rangle$ since the magnitudes of coefficients A & B and phase ϕ between the two states are controlled by the orientation of the pump beam HWP and quartz plate (shown in figure 3.1), respectively [2].

Three tests of local realism, namely Freedman’s test, CHSH test and Hardy’s test, were conducted. Each of the tests employed a different mathematical framework upon which local realism was tested.

For Freedman’s & CHSH test, the entangled state $|\Phi^+\rangle$ represented by equation 3.3 was generated using the method outlined in section 3.1.2. $|\Phi^+\rangle$ is one of the four famous maximally entangled Bell states.

$$|\Phi^+\rangle = \frac{1}{\sqrt{2}} |HH\rangle + \frac{1}{\sqrt{2}} |VV\rangle. \quad (3.3)$$

For Hardy’s test, the entangled state $|\Psi\rangle$ represented by equation 3.4 was generated using the method outlined in section 3.3.1.

$$|\Psi\rangle = \sqrt{0.2} |HH\rangle + \sqrt{0.8} |VV\rangle. \quad (3.4)$$

The underlying logic for generation of these particular states is expressed in the relevant section for each test.

3.1 Freedman's test of local realism

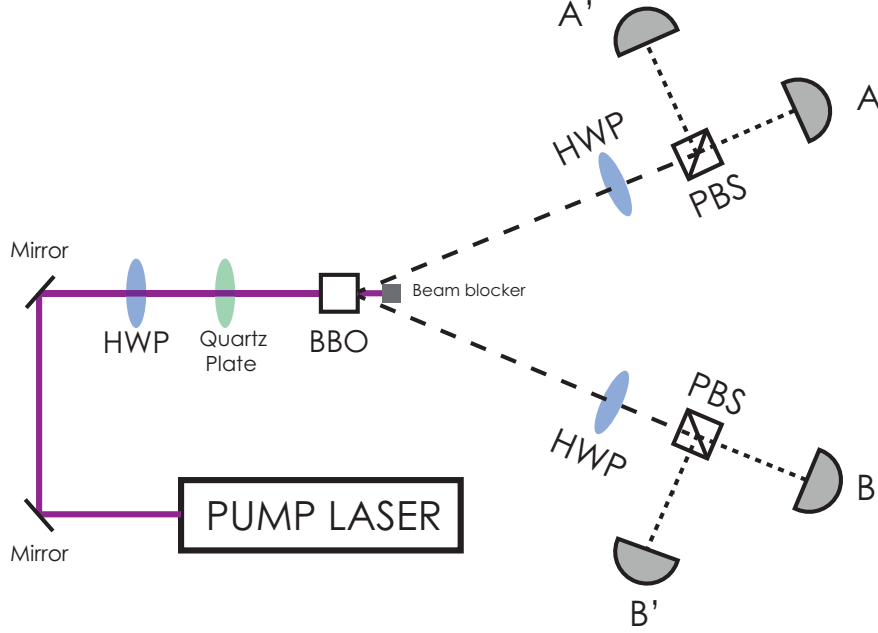


Figure 3.2: Instead of the two-detector arrangement suggested in [2] a four-detector arrangement was employed for Freedman's test. This setup was used to generate the state $|\Phi^+\rangle$. The combination of HWP + PBS in both channels enacts the working of a polarizer. Since the effective polarizer combination consists of a HWP and a polarizing beam splitter instead of a polarizer, the channel HWP needs to be rotated at half the analysis angles with respect to the horizontal [2].

The first experiment probing quantum entanglement & nonlocality performed was Freedman's test. The *testing parameter* employed in this test was the quantity δ defined by equation 3.5 [2],

$$\delta = \left| \frac{N(22.5^\circ) - N(67.5^\circ)}{N_0} \right| - \frac{1}{4}, \quad (3.5)$$

where $N(\phi)$ are the coincidence counts when the relative angle between the two *effective polarizer* combinations is ϕ and N_0 represents the coincidence counts recorded with no *effective polarizer* components present in both the channels/beams. δ was labelled the *testing parameter* since it would allow us to deduce whether local realism has been obeyed or violated. On inspecting equation 3.5 it can be inferred that δ can directly be determined from the coincidence counts data. Hence equation 3.5 will be utilized to determine the experimental value of δ , δ_{exp} .

Quantum mechanical prediction for the quantity δ defines it as [2],

$$\delta = \frac{\epsilon_A \epsilon_B}{2\sqrt{2}} - \frac{1}{4}, \quad (3.6)$$

where ϵ_A & ϵ_B represent the transmittance of the polarizer present in channel A(signal) and channel B(idler), respectively. Since the combination of a HWP & a polarizing beam splitter was utilized to enact the function of a polarizer in both channels, in this case ϵ_A represents the transmittance of the *effective polarizer* combination in channel A(signal) and ϵ_B represents the transmittance of

the *effective polarizer* combination in channel B(idler) .

Assuming locality, reality and hidden variable arguments are obeyed, δ attains a value ≤ 0 [2]. This inequality is referred to as *Freedman's inequality*, and puts a constraint on the values of δ if local realism is to be obeyed. An entangled state, which in theory defies the aforementioned assumptions of locality, reality and hidden variable arguments, should violate the aforementioned Freedman's inequality,

$$\delta \leq 0, \quad (3.7)$$

and obtain a value > 0 . This is the premise underpinning our experiment. Equation 3.6 can be used to calculate the theoretical value of δ if the transmittances ϵ_A & ϵ_B are known. Hence to determine the range in which our experimental value of δ should lie to successfully violate local realism we first need to determine ϵ_A & ϵ_B .

To determine the transmittances, the setup shown in figure 3.3 was used. In the SPDC setup shown in figure 2.5, a two-detector arrangement was utilized whereas the entanglement experiments and the determination of transmittances require a four-detector setup. Hence, the setup shown in figure 2.5 was updated to the setup shown in figure 3.3. Since two more detectors, detectors A' & B' were added these needed to be aligned before we could determine the respective transmittances of the *effective polarizers*. The alignment procedure carried out for these detectors is laid out in section 3.1.1. With all the detectors aligned, the transmittances for both our *effective polarizers* were determined and had the following magnitudes,

$$\begin{aligned} \epsilon_A &= 0.975 \pm 0.006, \\ \epsilon_B &= 0.995 \pm 0.008. \end{aligned}$$

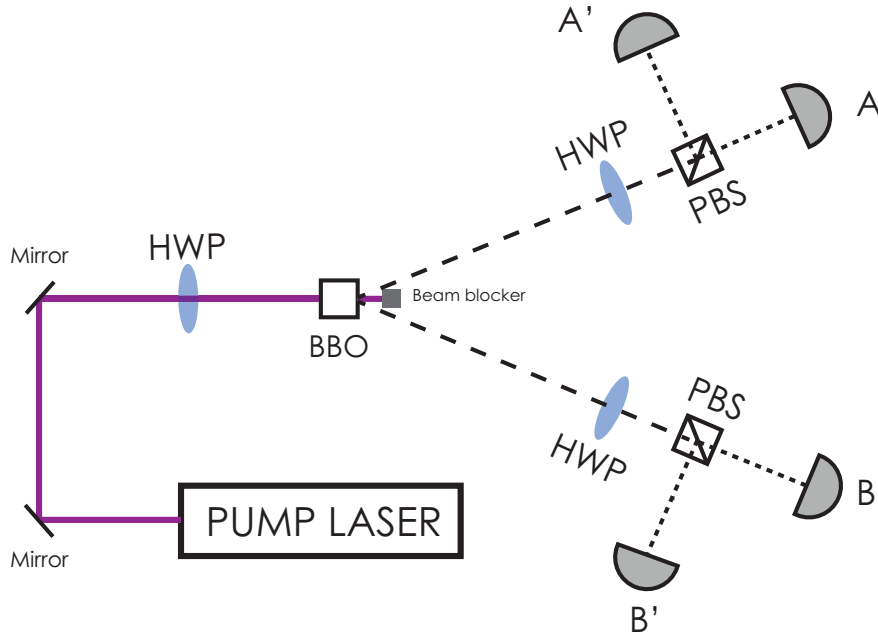


Figure 3.3: Experimental arrangement used to determine ϵ_A & ϵ_B .

Using the values of ϵ_A , ϵ_B and equation 3.6, the theoretical value of δ comes out to be,

$$\delta_{theo} = 0.0932 \pm 0.0003.$$

This suggests that a successful violation of local realism (equivalent to violating Freedman's inequality) demands our experimental value of δ , δ_{exp} lie in the range specified by equation 3.8,

$$0 < \delta_{exp} \leq \delta_{theo}, \quad (3.8)$$

$$0 < \delta_{exp} \leq 0.0932 \pm 0.0003. \quad (3.9)$$

3.1.1 Aligning the four detector arrangement

For all the entanglement experiments, the four-detector arrangement shown in 3.1 was required. This demands an increase from the number of detectors last used in studying SPDC. Provided detectors A & B utilized in the SPDC experimental arrangement (shown in figure 2.5) are still aligned, the added detectors A' & B' had to be aligned before the four-detector arrangements' prowess could be utilized. The detector B' was aligned first and then following the same routine the detector A' was aligned.

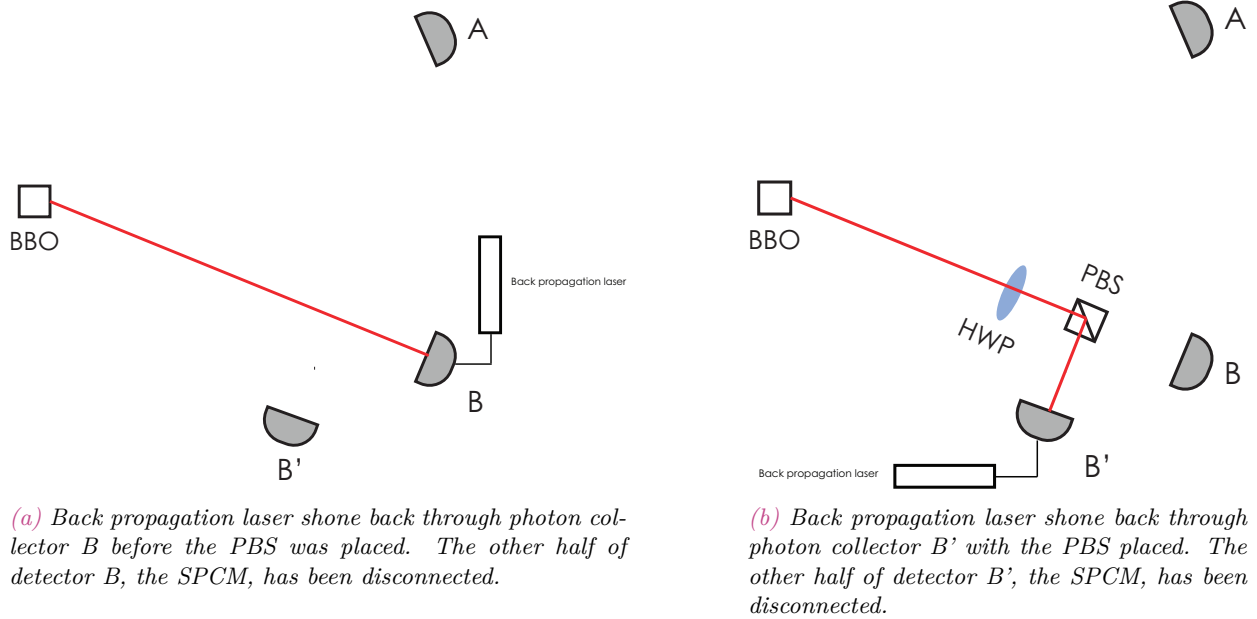


Figure 3.4: Back propagation setups utilized to coarsely align detectors B, B' and the PBS for the four-detector arrangement.

The pump laser is turned off and the optical fiber connecting the photon collector B and its respective SPCM is disconnected and the back-propagation laser is shone back towards the center of the BBO stack as shown in figure 3.4a. A PBS is then placed in the path of the back propagation laser and tweaked until the back propagation laser emerges exactly from the center of the other face of the PBS. It is ensured that this face of the PBS facing the BBO stack is perpendicular to the emerging laser. Now the detector B' is placed perpendicularly from the reflection end of the PBS and it is ensured that the detectors B and B' are both equidistant from the PBS. The optical

fiber connecting the photon collector B' and its respective SPCM is disconnected and the back-propagation laser is shone back towards the reflection end of the PBS from the photon collector B'. It is ensured that the back propagation laser is reflected and emerges from the center of the face of the PBS facing the BBO stack. As shown in 3.4b, a HWP is now inserted close to the PBS such that the back propagation laser passes through its center as well and is still incident on the center of the BBO stack. Two back propagation lasers are simultaneously shone back from photon collectors B and B' towards the BBO stack as shown in figure 3.5.

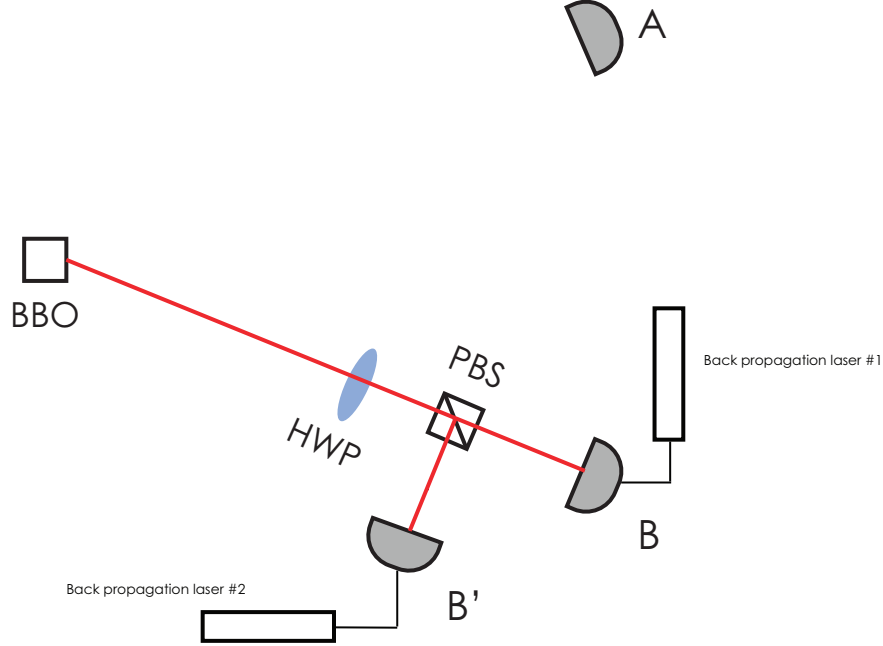


Figure 3.5: Two back propagation lasers shone backwards towards the BBO stack to fine-tune the coarse alignment of detector B'.

Minor tweaks are made so that both the lasers coincide exactly at the center of the BBO stack. This completes the coarse alignment of detector B'. The back propagation lasers are disconnected and the optical fibers between the photon collectors & their respective SPCMs are connected back.

To fine-tune and complete the alignment of detector B', we turn the pump laser on and set the pump beam HWP at 45° so that the down-converted photons produced are in the state $|VV\rangle$. Since $|V\rangle$ photons are transmitted through the PBS, maximal single counts are observed on detector B. At the same time maximum coincidence counts AB are observed on the counting software. The pump beam HWP is now set at 0° so that down-converted $|HH\rangle$ photons are being produced. Since $|H\rangle$ photons are reflected by the PBS, maximal single counts are observed on detector B'. At the same time maximum coincidence counts AB' are observed on the counting software. Since detector B was already aligned, the maximum AB coincidence counts were used as a reference to compare the maximum AB' coincidence counts. No significant difference was observed in these as ideally should be the case. This completes fine alignment of detectors B and B', following similar routine the detector A' was aligned, since detector A was already aligned. It is suggested in [2] that the maximum of coincidence counts AB and the maximum of coincidence counts AB' should not be significantly different. If a significant difference is observed, then alignment may need to be improved or re-done. The optic fibres for one of the B and B' detectors may also need cleaning, or it might be the case that the fibre coupling lens for one of the detectors may have a better alignment

than that of the other.

With all the detectors in the four-detector arrangement aligned, we can proceed taking no prisoners with the entanglement experiments.

3.1.2 Generating the state $|\Phi^+\rangle$

For Freedman's and CHSH test we would like to generate the state $|\Phi^+\rangle$, since it is one of the four maximally entangled Bell states represented by equations 3.10 - 3.13,

$$|\Phi^+\rangle = \frac{1}{\sqrt{2}} |HH\rangle + \frac{1}{\sqrt{2}} |VV\rangle, \quad (3.10)$$

$$|\Phi^-\rangle = \frac{1}{\sqrt{2}} |HH\rangle - \frac{1}{\sqrt{2}} |VV\rangle, \quad (3.11)$$

$$|\psi^+\rangle = \frac{1}{\sqrt{2}} |HV\rangle + \frac{1}{\sqrt{2}} |VH\rangle, \quad (3.12)$$

$$|\psi^-\rangle = \frac{1}{\sqrt{2}} |HV\rangle - \frac{1}{\sqrt{2}} |VH\rangle. \quad (3.13)$$

To generate $|\Phi^+\rangle$, the four-detector arrangement shown in figure 3.1 was used. Considering the general two-photon state represented by equation 3.2, it can be seen to get the state $|\Phi^+\rangle$ we need the coefficients A & B in equation 3.2 to be $= \frac{1}{\sqrt{2}}$ and the phase ϕ to be $= 0$. To accomplish the first condition, *effective polarizers* A and B are set at 0° to observe the $|HH\rangle$ counts (A'B' counts) and the pump beam HWP is adjusted such that the coincidence counts (AB counts), on setting the *effective polarizers* at 90° (in our case this is equivalent to setting the channel HWPs to half the magnitude of the required angle i.e. 90°), are approximately equal. It is ensured that for cross-orientations of the *effective polarizers* i.e. one *effective polarizer* set at 0° and the other at 90° and vice versa, we get minimum AB coincidence counts. With these steps undertaken, the $|HH\rangle$ and $|VV\rangle$ counts in the $\{|H\rangle, |V\rangle\}$ basis had been approximately equalized ($\approx 1 : 1$ ratio) and the counts $|HV\rangle$ and $|VH\rangle$ had been minimized. With these requisites met, the coefficient $A = B = \frac{1}{\sqrt{2}}$ and the general state $|\psi\rangle$ had been transformed to the state $|\psi\rangle_{trans}$, equation 3.14 displays this transformation,

$$|\psi\rangle = A |HH\rangle + B e^{i\phi} |VV\rangle \implies |\psi\rangle_{trans} = \frac{1}{\sqrt{2}} |HH\rangle + \frac{1}{\sqrt{2}} e^{i\phi} |VV\rangle. \quad (3.14)$$

To get the state $|\Phi^+\rangle$ from the $|\psi\rangle_{trans}$ state, phase ϕ needs to be $= 0$. The first step is to change the measurement basis to the $\{|D\rangle, |A\rangle\}$ basis. The state $|D\rangle$ is the diagonally polarized state represented in the $\{|H\rangle, |V\rangle\}$ basis as,

$$|D\rangle = \frac{1}{\sqrt{2}} (|H\rangle + |V\rangle). \quad (3.15)$$

Whereas the state $|A\rangle$ is the anti-diagonal polarization state represented in the $\{|H\rangle, |V\rangle\}$ basis as,

$$|A\rangle = \frac{1}{\sqrt{2}} (|H\rangle - |V\rangle). \quad (3.16)$$

Now to change our basis to the $\{|D\rangle, |A\rangle\}$ basis we need to upgrade our four-detector arrangement by further incorporating a QWP shown in *basis changing* combination of components displayed in figure 3.6.

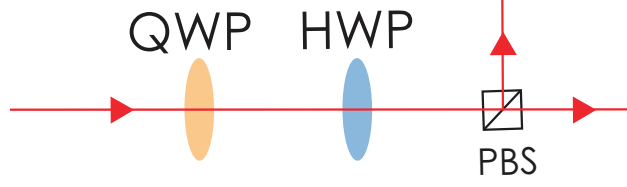
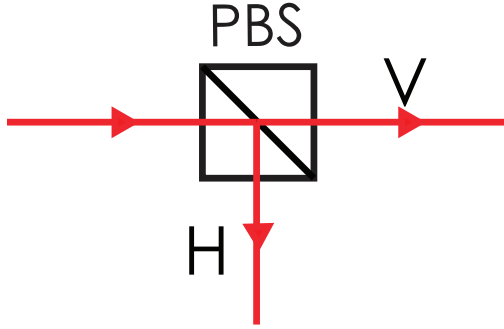
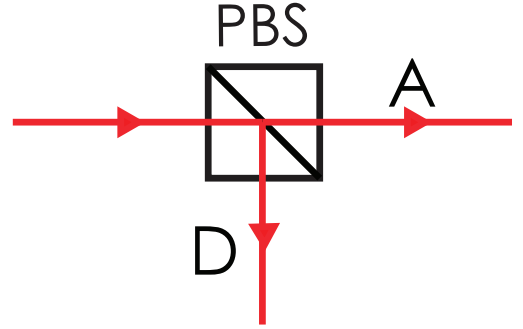


Figure 3.6: This arrangement of components can be utilized to change our measurement basis to the required basis.

With the QWP added to our four-detector arrangement shown in figure 3.1, we could change the measurement basis to the $\{|D\rangle, |A\rangle\}$ by orienting the QWP and HWP at 45° and 22.5° , respectively. The state $|D\rangle$ has been *rotated* to the state $|H\rangle$. This implies that counts corresponding to $|D\rangle$ photons would be detected at the same detector at which the $|H\rangle$ counts were being detected. A conceptual illustration extending this concept is shown in figure 3.7.



(a) A $|H\rangle, |V\rangle$ PBS which transmits the vertically polarized photons $|V\rangle$ and reflects the horizontally polarized photons $|H\rangle$.



(b) An imaginative $|D\rangle, |A\rangle$ PBS which transmits the diagonally polarized photons $|D\rangle$ and reflects the anti-diagonally polarized photons $|A\rangle$.

Figure 3.7: Working of the $|H\rangle, |V\rangle$ (figure 3.7a) and imaginative $|D\rangle, |A\rangle$ (figure 3.7b) beam splitters. Changing the measurement basis to the $\{|D\rangle, |A\rangle\}$ basis and immediately putting a $|H\rangle, |V\rangle$ PBS after the HWP as shown in figure 3.6 enacts the working of a $|D\rangle, |A\rangle$ PBS shown in figure 3.7b.

Once the measurement basis had been changed to the $\{|D\rangle, |A\rangle\}$ basis, the *effective polarizers* A and B were oriented at 45° and -45° , respectively (in our case this corresponds to setting the channel HWPs A and B to half the magnitudes of the required angles i.e. 22.5° and -22.5° , respectively). Now the tilt of the quartz plate about the vertical axis was adjusted such that the AB coincidence counts were minimized. After this minimization of AB counts is achieved, orientations of the *effective polarizers* A and B were interchanged to -45° and 45° , respectively. It was ensured that AB coincidences were still at a minimum. Once these steps had been carried out, the phase ϕ was at a minimum, implying that the state $|\psi\rangle_{trans}$ had been transformed to the maximally entangled state $|\Phi^+\rangle$ as shown below,

$$|\psi\rangle_{trans} = \frac{1}{\sqrt{2}} |HH\rangle + \frac{1}{\sqrt{2}} e^{i\phi} |VV\rangle \Rightarrow |\Phi^+\rangle = \frac{1}{\sqrt{2}} |HH\rangle + \frac{1}{\sqrt{2}} |VV\rangle.$$

The QWP incorporated for changing the measurement basis was removed from the four-detector arrangement after ϕ had been minimized.

3.1.3 Experiment & results

The state $|\Phi^+\rangle$ was generated following the routine outline in section 3.1.2. Employing the four-detector arrangement shown in figure 3.2, the coincidence counts in equation 3.5, $N(22.5^\circ)$, $N(67.5^\circ)$ and N_0 were recorded. A 30 s data acquisition was carried out for each iteration of recording the aforementioned counts. Once these counts had been determined, their values were plugged in equation 3.5 and δ_{exp} was calculated. The statistics and results obtained are summarized in table 3.1.

Time	$N(22.5^\circ)$	$N(67.5^\circ)$	N_0	δ_{exp}	Confidence
30 s	2987 ± 8	522 ± 4	7281 ± 16	0.08864 ± 0.0004	219σ

Table 3.1: Data and results obtained for Freedman's test.

The experimental value of δ is greater than 0,

$$\begin{aligned} \delta_{exp} &> 0, \\ 0.08864 \pm 0.0004 &> 0. \end{aligned}$$

This affirms that the photon pairs under consideration were entangled and violated local realism since Freedman's inequality (equation 3.7) has been violated.

3.2 CHSH test of local realism

The second experiment performed was the CHSH test. The testing parameter employed in this test was the quantity S defined by equation 3.17 [2],

$$S = E(a, b) - E(a, b') + E(a', b) + E(a', b'), \quad (3.17)$$

where $E(x, y)$, a quantity which represents the expected outcome of a local realistic measurement for the analysis angle of x in channel A(signal) and y in channel B(idler), is defined as [2],

$$E(x, y) = P_{HH} + P_{VV} - P_{HV} - P_{VH} = \cos(2(x - y)). \quad (3.18)$$

S would allow us to deduce whether local realism has been obeyed or violated. Assuming locality, reality and hidden variable arguments are obeyed, $|S|$ attains a value ≤ 2 [2]. This is referred to as *The CHSH inequality*. An entangled state, which in theory defies the aforementioned assumptions, should violate the classical prediction put forth by the the aforementioned CHSH inequality,

$$|S| \leq 2. \quad (3.19)$$

Since $|\Phi^+\rangle$ is maximally entangled, we should expect maximum violation of the CHSH inequality. Using equations 3.18 & 3.17 and the following values of analysis angles ($a = -45^\circ$, $a' = 0^\circ$, $b = 22.5^\circ$, $b' = -22.5^\circ$), we compute the theoretical value of S for $|\Phi^+\rangle$ to be,

$$S_{theo} = 2\sqrt{2}.$$

Owing to experimental constraints, it is non-trivial to exactly generate $|\Phi^+\rangle$. This implies that a successful violation of the CHSH inequality (equivalent to a proof of non-locality) demands our experimentally determined value of S lie in the range given by equation 3.20,

$$\begin{aligned} 2 < S_{exp} < S_{theo}, \\ 2 < S_{exp} < 2\sqrt{2}. \end{aligned} \tag{3.20}$$

3.2.1 Experiment & results

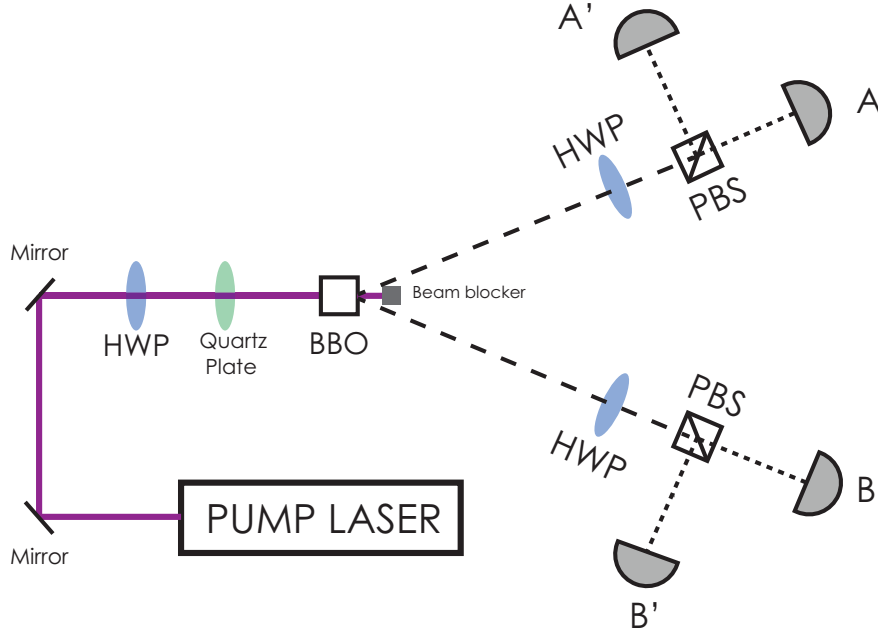


Figure 3.8: A four-detector experimental arrangement for the CHSH test. This setup was used to generate the state $|\Phi^+\rangle$. The combination of HWP + PBS in both channels enacts the working of a polarizer. Since the effective polarizer combination consists of a HWP and a polarizing beam splitter instead of a polarizer, the channel HWP needs to be rotated at half the analysis angles with respect to the horizontal [2].

To perform the test, the state $|\Phi^+\rangle$ (one of the four Bell states) was experimentally generated following the same routine outlined in section 3.1.2. The state $|\Phi^+\rangle$ was generated because theoretically it is predicted to violate the CHSH inequality the most.

As required by equation 3.17, to calculate S we need to determine $E(x, y)$ for four sets of analysis angle pairs: (a, b) , (a, b') , (a', b) , (a', b') . This was achieved by setting the channel HWPs to half the values of the analysis angles ($a = -45^\circ$, $a' = 0^\circ$, $b = 22.5^\circ$, $b' = -22.5^\circ$) for each analysis angle pair and collecting the corresponding coincidence counts data. The data collected was used to determine the probabilities mentioned in equation 3.18, which consequently allowed us to determine $E(a, b)$, $E(a, b')$, $E(a', b)$, $E(a', b')$. Once $E(x, y)$ had been determined for each set of analysis angle pairs, equation 3.17 allowed us to determine the experimental value of S , S_{exp} . Three runs for this test were performed, with increasing data acquisition time in each run. This

was done to improve the confidence interval of the results. The results obtained are presented in table 3.2.

Time	S_{exp}	Confidence
30 s	2.608 ± 0.005	118 σ
60 s	2.610 ± 0.004	158 σ
120 s	2.604 ± 0.003	219 σ

Table 3.2: Results for the CHSH test.

All three experimental values of S lie in the range specified by equation 3.20,

$$\begin{aligned}
2 &< S_{exp} < S_{theo}, \\
2 &< 2.608 \pm 0.005 < 2\sqrt{2}, \\
2 &< 2.610 \pm 0.004 < 2\sqrt{2}, \\
2 &< 2.604 \pm 0.003 < 2\sqrt{2}.
\end{aligned}$$

This affirms that the photon pairs under consideration were entangled and violated local realism since the CHSH inequality (equation 3.19) has been violated by each value of S_{exp} .

3.3 Hardy's test of local realism

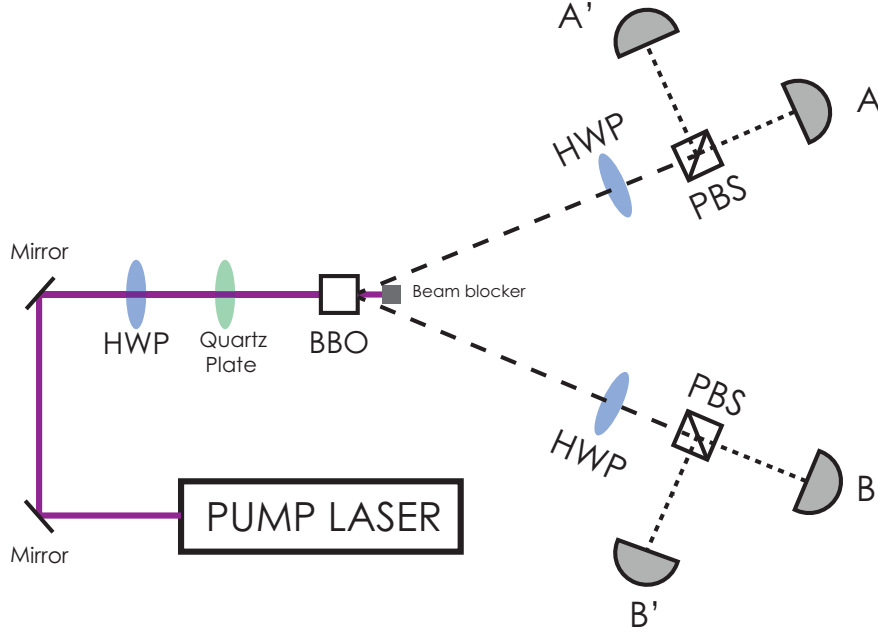


Figure 3.9: A four-detector arrangement was employed for Hardy's test. This setup was used to generate the state $|\Psi\rangle$. The combination of HWP + PBS in both channels enacts the working of a polarizer. Since the effective polarizer combination consists of a HWP and a polarizing beam splitter instead of a polarizer, the channel HWP needs to be rotated at half the analysis angles with respect to the horizontal [2].

The last experiment performed was Hardy's test. The testing parameter employed in this test was the quantity H defined by equation 3.21 [2],

$$H = P(\beta, -\beta) - P(\beta, \alpha^\perp) - P(-\alpha^\perp, -\beta) - P(-\alpha, \alpha), \quad (3.21)$$

where $P(X_A, Y_B)$, a quantity which represents the joint probability of detecting photons which reach detectors A & B and are polarized along angles X and Y , is defined as [2],

$$P(X_A, Y_B) = \frac{N_{AB}}{N_{AB} + N_{AB'} + N_{A'B} + N_{A'B'}}. \quad (3.22)$$

Similarly, other relevant probabilities have been defined below,

$$P(X_A, Y_{B'}) = \frac{N_{AB'}}{N_{AB} + N_{AB'} + N_{A'B} + N_{A'B'}}, \quad (3.23)$$

$$P(X_{A'}, Y_B) = \frac{N_{A'B}}{N_{AB} + N_{AB'} + N_{A'B} + N_{A'B'}}, \quad (3.24)$$

$$P(X_{A'}, Y_{B'}) = \frac{N_{A'B'}}{N_{AB} + N_{AB'} + N_{A'B} + N_{A'B'}}. \quad (3.25)$$

H was labelled the *testing parameter* since it would allow us to deduce whether local realism has been obeyed or violated. On inspecting equation 3.21 it can be inferred that H can be determined

if the probabilities, $P(\beta, -\beta)$, $P(\beta, \alpha^\perp)$, $P(-\alpha^\perp, -\beta)$, $P(-\alpha, \alpha)$ are known. By setting the *effective polarizers* to the following analysis angle pairs: $(\beta, -\beta)$, (β, α^\perp) , $(-\alpha^\perp, -\beta)$, $(-\alpha, \alpha)$ and recording the coincidence counts data, the aforementioned probabilities can be determined using equations 3.22 - 3.25. Equation 3.21 can then be utilized to determine the experimental value of H , H_{exp} . Note that since the combination of a HWP and a PBS is being used to enact the function of a polarizer in both channels A and B (figure 3.9), the channel HWPs need to be rotated at half the analysis angles with respect to the horizontal [2].

Quantum mechanical considerations [2] allow us to define the joint probability $P(X_A, Y_B)$ as,

$$P(X_A, Y_B) = (A \cos X_A \cos Y_B + B \sin X_A \sin Y_B)^2. \quad (3.26)$$

Assuming locality, reality and hidden variable arguments are obeyed, H attains a value ≤ 0 [2]. This inequality is referred to as *Hardy's inequality*, and puts a constraint on the values H can attain if local realism is to be satisfied. Using equation 3.26, it can be verified that maximal violation of Hardys inequality can be achieved with state $|\Psi\rangle$ (defined by equation 3.4). The analysis angles for this state are $\alpha = 35^\circ$ & $\beta = 19^\circ$ [2]. Using $A = B = \frac{1}{\sqrt{2}}$ & $\phi = 0$ in the general two-photon state described by equation 3.2 and choosing $\alpha = 35^\circ$ & $\beta = 19^\circ$, equations 3.21 and 3.26 gave us the following prediction for H ,

$$H_{theo} = 0.093.$$

Hence, the state $|\Psi\rangle$ should violate local realism since $H_{theo} > 0$.

3.3.1 Generating the state $|\Psi\rangle$

For Hardy's test we would like to generate the state $|\Psi\rangle$, since theoretically it violates Hardy's inequality the most. To generate $|\Phi^+\rangle$, the four-detector arrangement shown in figure 3.9 was used. Considering the general two-photon state represented by equation 3.2, it can be seen to get the state $|\Psi\rangle$ we need the coefficients A & B in equation 3.2 to be $= \sqrt{0.2}$ & $\sqrt{0.8}$ respectively and furthermore we need the phase ϕ to be $= 0$. To accomplish the first condition, *effective polarizers* A and B are set at 0° to observe the $|HH\rangle$ counts (A'B' counts) and the pump beam HWP is adjusted such that the coincidence counts on setting the *effective polarizers* at 90° (AB counts, corresponding to detecting $|VV\rangle$ photons), are approximately in a 4 : 1 ratio. In our case, the channel HWPs need to be oriented at half the magnitude of the required angle(s) since we're not using a polarizer. By undertaking the steps outlined our coefficients A & B take on the desired values. Now to arrive at $|\Psi\rangle$, we need to minimize phase ϕ . This was done by following the same Ψ minimization routine outlined in section 3.1.2. By this point, the general two-photon state had been successfully transformed into the required $|\Psi\rangle$ state. This transformation is depicted by equation 3.27,

$$|\psi\rangle = A|HH\rangle + Be^{i\phi}|VV\rangle \implies |\Psi\rangle = \sqrt{0.2}|HH\rangle + \sqrt{0.8}|VV\rangle. \quad (3.27)$$

3.3.2 Experiment & results

The state $|\Psi\rangle$ was generated following the routine outline in section 3.3.1. Employing the four-detector arrangement shown in 3.9, the coincidence counts data relevant for each probability present in equation 3.21 was acquired over an interval of 120 s. The coincidence counts data recorded was

used to calculate the aforementioned probabilities using equations 3.22 - 3.25. The calculated probabilities are shown in table 3.3.

$P(\beta, -\beta)$	$P(\beta, \alpha^\perp)$	$P(-\alpha^\perp, -\beta)$	$P(-\alpha, \alpha)$
0.1122 ± 0.0004	0.0217 ± 0.0002	0.0187 ± 0.0002	0.0329 ± 0.0002

Table 3.3: Probabilities calculated to determine H_{exp} for Hardys test.

Once the probabilities had been calculated, equation 3.21 was utilized to calculate the experimental value of H , H_{exp} . The result(s) obtained are displayed in table 3.4.

Time	H_{exp}	Confidence
120 s	0.0389 ± 0.0005	71 σ

Table 3.4: Results for Hardys test.

The experimental value of H is greater than 0,

$$H_{exp} > 0,$$

$$0.0389 \pm 0.0005 > 0.$$

This affirms that the photon pairs under consideration were entangled and violated local realism since Hardys inequality has been violated.

Quantum state tomography

What we observe is not nature in itself but nature exposed to our method of questioning'

Werner Heisenberg

Quantum state tomography is a technique concerned with estimating a quantum state. It accomplishes this by undertaking carefully orchestrated measurements [2]. Based on these measurements, It aims to construct a *special* matrix called the *density matrix*. This *special* matrix can be used to represent both pure & mixed quantum states.

This chapter deals with the experimental procedure utilized to perform two-qubit quantum state tomography. However, before exploring QST experimentally, I reckon it is essential to briefly describe the theoretical underpinnings which form the basis of this technique. This provides essential context needed to understand the experiment.

4.1 Theoretical background

4.1.1 The density matrix formalism

A pure quantum state is the state in which exact information of the system is known. Pure states can be represented as state vectors $|\psi\rangle$ in the elegant bra-ket notation. All the states described (including the entangled & superposition states) until now are pure states. However, sometimes the system under consideration can be prepared as the statistical ensemble of two or more pure states. In this case, the system is said to be in a *mixed* state. For e.g. the states $|H\rangle$ and $|V\rangle$, each with probability 50% can be *mixed* together to form a mixed state. This mixed state is not to be confused with the pure superposition state $|D\rangle$ represented by equation 3.15.

When the pure state $|D\rangle$ is considered, the system is simultaneously in both $|H\rangle$ **and** $|V\rangle$ states before a measurement is made. Assuming the states $|H\rangle$ and $|V\rangle$ form an orthonormal basis, there is a 50% chance of getting $|H\rangle$ and a 50% chance of getting $|V\rangle$ when a measurement on $|D\rangle$ is made in the $\{|H\rangle, |V\rangle\}$ basis. Now a mixed state consisting of 50% $|H\rangle$ states and 50% $|V\rangle$ states is considered. If a system is randomly *drawn* from the mixture then the system is either in the $|H\rangle$ **or** the $|V\rangle$ state. If it's found to be in the $|H\rangle$ state, then on performing a measurement in the $\{|H\rangle, |V\rangle\}$ basis there is a 100% chance of getting $|H\rangle$ and vice versa. At no point in this example the system existed simultaneously in both $|H\rangle$ **and** $|V\rangle$ states. This, hopefully, illustrates the difference between a mixed state and a pure superposition state.

Unlike pure states, mixed states cannot be represented by kets [2]. To describe mixed states the *density matrix* formalism is used. In this formalism, the density matrix $\hat{\rho}$ defined in equation 4.1 is used to represent a quantum state. The density matrix formalism can be used to represent both mixed and pure states.

$$\hat{\rho} = \sum_i p_i |\psi_i\rangle \langle \psi_i|, \quad (4.1)$$

here p_i represents the probability of getting the respective state $|\psi_i\rangle$ from the mixed state ($p_i = P(|\psi_i\rangle)$). These probabilities must lie in the range $0 \leq p_i \leq 1$ and be normalized $\sum_i p_i = 1$. For

pure states, the density matrix $\hat{\rho}$ can trivially be devised as $|\psi\rangle\langle\psi|$. This implies that the density matrix of a mixed state is a probability-weighted superposition of density matrices of pure states [2]. A legitimate density matrix must have the following properties:

- Trace $Tr(\hat{\rho}) = 1$.
- Be positive definitive.
- $\hat{\rho}^\dagger = \hat{\rho}$.
- $\hat{\rho}^2 \leq 1$.

4.1.2 Two-qubit states & theory governing two-qubit QST

A qubit is described as a two-level quantum system since. It can exist simply either as the $|0\rangle$ state or the $|1\rangle$ state or as superposition of these states [2]. A single-qubit quantum state is described by equation 4.2,

$$|\psi\rangle = \alpha |0\rangle + \beta |1\rangle, \quad (4.2)$$

where the probability coefficients $|\alpha|^2 + |\beta|^2 = 1$. Similarly, a two-qubit quantum state can be written as,

$$|\psi\rangle = \gamma_0 |00\rangle + \gamma_1 |01\rangle + \gamma_2 |10\rangle + \gamma_3 |11\rangle, \quad (4.3)$$

where the probability coefficients $\sum_{i=0}^3 |\gamma_i|^2 = 1$. This two-qubit state lives in a four-dimensional space and can be represented by a column vector as follows [2],

$$\begin{pmatrix} \gamma_0 \\ \gamma_1 \\ \gamma_2 \\ \gamma_3 \end{pmatrix}.$$

Employing the column vector approach to represent polarization states of photons and the general two-qubit state described in equation 4.3, an arbitrary two-photon pure state in the $\{|H\rangle, |V\rangle\}$ basis can be written as [2],

$$|\psi\rangle = \eta_0 |HH\rangle + \eta_1 |HV\rangle + \eta_2 |VH\rangle + \eta_3 |VV\rangle = \begin{pmatrix} \eta_0 \\ \eta_1 \\ \eta_2 \\ \eta_3 \end{pmatrix}. \quad (4.4)$$

Using the density matrix formalism, the generalized mixed state can be described by the following density matrix [2],

$$\hat{\rho}_{gen} = \begin{bmatrix} A_1 & B_1 e^{i\phi_1} & B_2 e^{i\phi_2} & B_3 e^{i\phi_3} \\ B_1 e^{-i\phi_1} & A_2 & B_4 e^{i\phi_4} & B_5 e^{i\phi_5} \\ B_2 e^{-i\phi_2} & B_4 e^{-i\phi_4} & A_3 & B_6 e^{i\phi_6} \\ B_3 e^{-i\phi_3} & B_5 e^{-i\phi_5} & B_6 e^{-i\phi_6} & A_4 \end{bmatrix}. \quad (4.5)$$

The definition of $\hat{\rho}_{gen}$ implies that determining $\hat{\rho}$ for an arbitrary two-photon state requires determining the perimeters (A_1, \dots, A_4) , (B_1, \dots, B_6) , (ϕ_1, \dots, ϕ_6) . Using the Pauli spin operators $\hat{\sigma}_0$, $\hat{\sigma}_1$, $\hat{\sigma}_2$, $\hat{\sigma}_3$ and the two-qubit S-coefficients defined in [2], the density matrix $\hat{\rho}$ can also be defined as,

$$\hat{\rho} = \frac{1}{4} \sum_{i,j=0}^3 S_{ij} (\hat{\sigma}_i \otimes \hat{\sigma}_j). \quad (4.6)$$

The S-coefficients S_{ij} , can directly be determined from joint probabilities, which in turn can be calculated from the photocounts measurements performed in the $\{|H\rangle, |V\rangle\}$, $\{|D\rangle, |A\rangle\}$ and $\{|R\rangle, |L\rangle\}$ bases. The state $|R\rangle$ is the right-circular polarization state represented in the $\{|H\rangle, |V\rangle\}$ basis as,

$$|R\rangle = \frac{1}{\sqrt{2}} (|H\rangle - i|V\rangle). \quad (4.7)$$

Whereas the state $|L\rangle$ is the left-circular polarization state represented in the $\{|H\rangle, |V\rangle\}$ basis as,

$$|L\rangle = \frac{1}{\sqrt{2}} (|H\rangle + i|V\rangle). \quad (4.8)$$

In a nutshell, to estimate the density matrix for an arbitrary two-qubit input state, we need to determine all 16 two-qubit S-coefficients [2]. For each qubit, we can use three settings corresponding to the three bases: $\{|H\rangle, |V\rangle\}$, $\{|D\rangle, |A\rangle\}$ and $\{|R\rangle, |L\rangle\}$. This means in total $3 \times 3 = 9$ settings (shown in table 4.1) are required. In each setting, four probabilities corresponding to the four output channels: $|HH\rangle$, $|HV\rangle$, $|VH\rangle$, $|VV\rangle$ need to be calculated. These measurements all together can then be used to construct $\hat{\rho}$ for the input state. Since three different measurement bases need to be setup, and in each basis joint probabilities corresponding to four output channels have to be determined, a four-detector arrangement similar to the one used in generating the $|\Psi\rangle$ & $|\Phi^+\rangle$ states needs to be employed.

As mentioned in [2], numerous sources of error are present in the setup. Even after these errors have been accounted for, it is highly likely that an *illegitimate density matrix* is obtained after carrying out the state estimation procedure. At this point, the *Maximum likelihood estimation* technique comes in handy. In essence, maximum likelihood estimation works by finding the state that is most likely to have resulted in the recorded photocounts. In our experiment, the online tomography interface developed by the Kwiat quantum information group was utilized for maximum likelihood estimation [5]. Figure 4.1 shows a screen-snap of the interface.

When counts in all the 9 aforementioned settings have been recorded, these recorded counts would be plugged into the interface. The interface, very conveniently, would carry out maximum likelihood estimation for us and return the *legitimate* density matrix $\hat{\rho}$ for the state which is most likely to have resulted in the recorded counts. Quantities of interest mentioned in section 4.1.3 can also be calculated using the same interface.

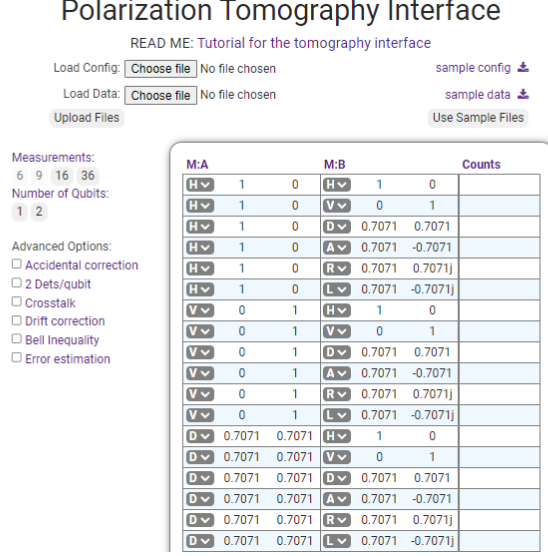


Figure 4.1: A screen-snap of the Kwiat information group's online tomography interface. This interface was used to carry out maximum likelihood estimation. For our experiment, the two-qubit & 36 measurement settings were ticked and then the recorded photocounts data was fed to the interface. <http://tomography.web.engr.illinois.edu/TomographyDemo.php>

4.1.3 Density matrix characterization quantities

Once $\hat{\rho}$ has been constructed for a state, different quantities of interest associated with $\hat{\rho}$ can be calculated. These quantities are defined as follows [2]:

- **Fidelity:** Measures the state overlap between two states $\hat{\rho}_1$ and $\hat{\rho}_2$. Fidelity $F(\hat{\rho}_1, \hat{\rho}_2) = \left(\text{Tr} \left[\sqrt{\sqrt{\hat{\rho}_1} \hat{\rho}_2 \sqrt{\hat{\rho}_1}} \right] \right)^2$. If we want to check how well a particular entangled state is generated, we can do quantum state tomography, obtain $\hat{\rho}$ of the generated state, and check its fidelity against the theoretical prediction [2].
- **Concurrence & Tangle:** Quantifies the entanglement of a system. For a two-qubit system, concurrence C is defined as,

$$C = \text{Max} \left\{ \sqrt{\lambda_1} - \sqrt{\lambda_2} - \sqrt{\lambda_3} - \sqrt{\lambda_4} \right\},$$

where $\lambda_1, \lambda_2, \lambda_3, \lambda_4$ are the eigenvalues of the matrix given by $\hat{\rho} \hat{Z} \hat{\rho}^T \hat{Z}$. Here \hat{Z} is the *spin*

flip matrix defined as $\begin{bmatrix} 0 & 0 & 0 & -1 \\ 0 & 0 & 1 & 0 \\ 0 & 1 & 0 & 0 \\ -1 & 0 & 0 & 0 \end{bmatrix}$. The tangle T can trivially be calculated using the following relation,

$$T = C^2.$$

Both concurrence and tangle range from 0 for non-entangled or mixed states to 1 for maximally mixed states [2].

4.2 Experiment & results

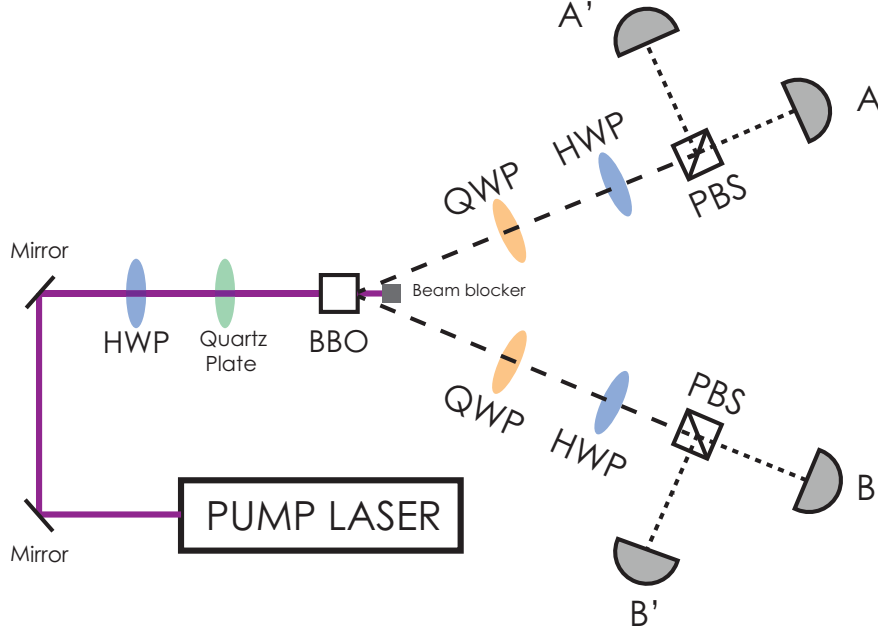


Figure 4.2: The four-detector arrangement shown above was employed for QST. The combination of pump HWP + quartz plate was used to generate the states for which $\hat{\rho}$ was to be constructed. The combination of HWP + QWP + PBS in each channel was used to setup the required measurement basis in each channel.

Using the combination of pump HWP & quartz plate(only utilized in generating $|\Phi^+\rangle$ and $|\Phi^+\rangle_\phi$ states), the following states were generated by essentially transforming the general two-photon state(equation 3.2) into the required states,

$$\begin{aligned}
 |\psi\rangle &= A|HH\rangle + Be^{i\phi}|VV\rangle \Rightarrow |HH\rangle, \\
 |\psi\rangle &= A|HH\rangle + Be^{i\phi}|VV\rangle \Rightarrow |VV\rangle, \\
 |\psi\rangle &= A|HH\rangle + Be^{i\phi}|VV\rangle \Rightarrow |\Phi^+\rangle = \frac{1}{\sqrt{2}}|HH\rangle + \frac{1}{\sqrt{2}}|VV\rangle, \\
 |\psi\rangle &= A|HH\rangle + Be^{i\phi}|VV\rangle \Rightarrow |\Phi^+\rangle_\phi = \frac{1}{\sqrt{2}}|HH\rangle - \frac{1}{\sqrt{2}}i|VV\rangle.
 \end{aligned}$$

The coefficients A & B in equation 3.2 are constrained by orientation of the pump HWP, whereas phase ϕ in equation 3.2 is controlled by orientation of the quartz plate.

States $|HH\rangle$ & $|VV\rangle$ were simply generated by orienting the pump HWP(refer figure 4.2) at 0° & 45° , respectively. To generate states $|\Phi^+\rangle$ & $|\Phi^+\rangle_\phi$, the routine used in section 3.1.2 was utilized, except, in generating $|\Phi^+\rangle_\phi$ the quartz plate was adjusted such that the phase ϕ was maximized. For each of the generated state, coincidence counts in each of the 9 measurement bases(shown in table 4.1) were recorded. The coincidence counts data recorded for each generated state was then fed into the tomography interface and $\hat{\rho}$ determined.

Measurement basis	Channel A HWP	Channel A QWP	Channel B HWP	Channel B QWP
$ HH\rangle$	0°	0°	0°	0°
$ HD\rangle$	0°	0°	22.5°	45°
$ HR\rangle$	0°	0°	0°	-45°
$ DH\rangle$	22.5°	45°	0°	0°
$ DD\rangle$	22.5°	45°	22.5°	45°
$ DR\rangle$	22.5°	45°	0°	-45°
$ RH\rangle$	0°	-45°	0°	0°
$ RD\rangle$	0°	-45°	22.5°	45°
$ RR\rangle$	0°	-45°	0°	-45°

Table 4.1: For each generated state, the coincidence photocounts were recorded in each of the above measurement bases. These recorded counts were then fed into the tomography interface shown in figure 4.1.

Both the theoretically predicted $\hat{\rho}$ and the experimentally determined $\hat{\rho}$ for the generated states are mentioned in the respective section of each state.

4.2.1 $|HH\rangle$ state

Theoretical prediction

$$\hat{\rho}_{theo} = \begin{bmatrix} 1 & 0 & 0 & 0 \\ 0 & 0 & 0 & 0 \\ 0 & 0 & 0 & 0 \\ 0 & 0 & 0 & 0 \end{bmatrix}$$

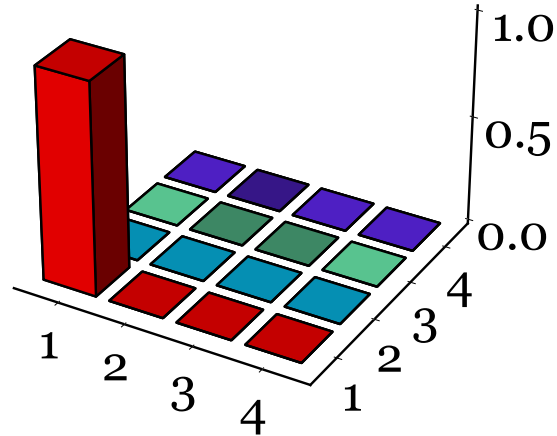


Figure 4.3: Magnitudes of $\hat{\rho}_{theo}$ elements for the $|HH\rangle$ state.

Experimental results

$$\hat{\rho}_{exp} = \begin{bmatrix} 0.989 & 0.0136 + 0.0346i & -0.0277 - 0.0473i & -0.000253 - 0.00403i \\ 0.0136 - 0.0346i & 0.00261 & -0.00167 + 0.0000142i & -0.000932 + 0.000343i \\ -0.0277 + 0.0473i & -0.00167 - 0.0000142i & 0.00323 & -0.000161 - 0.0000758i \\ -0.000253 + 0.00403i & -0.000932 - 0.000343i & -0.000161 + 0.0000758i & 0.00452 \end{bmatrix}$$

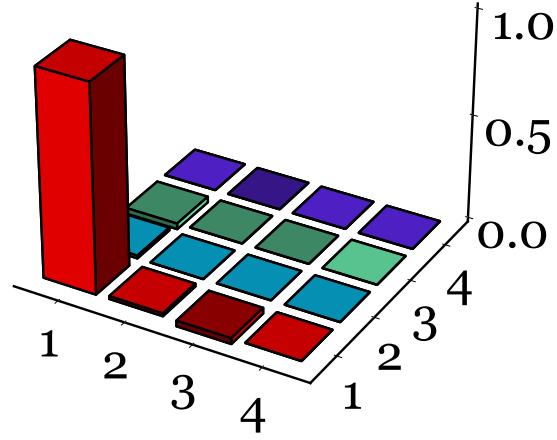


Figure 4.4: Magnitudes of $\Re(\hat{\rho}_{exp})$ elements for the $|HH\rangle$ state.

Fidelity	Concurrence	Tangle
0.990	0.00497	0.0000247

Table 4.2: Density matrix characterization quantities calculated for $\hat{\rho}_{exp}$ of $|HH\rangle$ state.

4.2.2 $|VV\rangle$ state

Theoretical prediction

$$\hat{\rho}_{theo} = \begin{bmatrix} 0 & 0 & 0 & 0 \\ 0 & 0 & 0 & 0 \\ 0 & 0 & 0 & 0 \\ 0 & 0 & 0 & 1 \end{bmatrix}$$

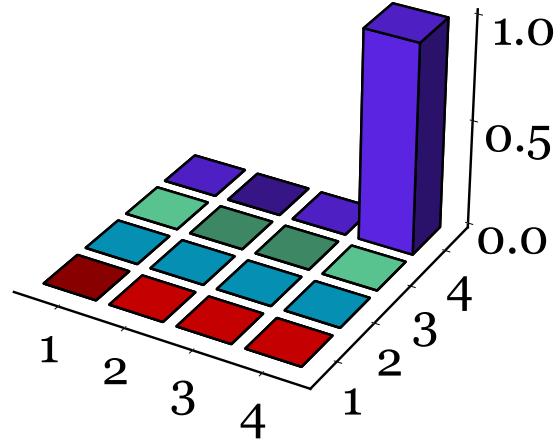


Figure 4.5: Magnitudes of $\hat{\rho}_{theo}$ elements for the $|VV\rangle$ state.

Experimental results

$$\hat{\rho}_{exp} = \begin{bmatrix} 0.0177 & 0.000969 - 0.000248i & -0.00169 + 0.00114i & 0.0106 + 0.00527i \\ 0.000969 + 0.000248i & 0.0147 & -0.00682 + 0.01i & 0.014 + 0.065i \\ -0.00169 - 0.00114i & -0.00682 - 0.01i & 0.0117 & 0.00758 - 0.0481i \\ 0.0106 - 0.00527i & 0.014 - 0.065i & 0.00758 + 0.0481i & 0.955 \end{bmatrix}$$

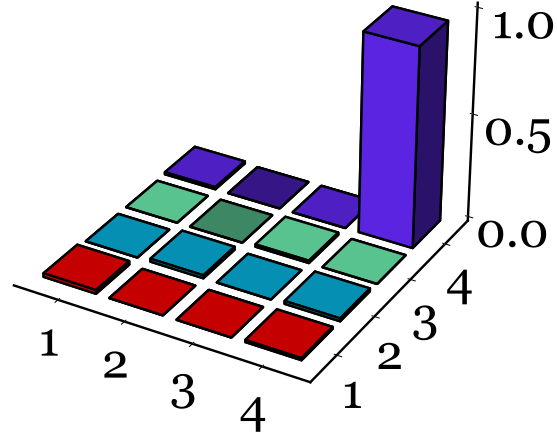


Figure 4.6: Magnitudes of $\Re(\hat{\rho}_{exp})$ elements for the $|VV\rangle$ state.

Fidelity	Concurrence	Tangle
0.956	0	0

Table 4.3: Density matrix characterization quantities calculated for $\hat{\rho}_{exp}$ of $|VV\rangle$ state.

4.2.3 $|\Phi^+\rangle$ state

Theoretical prediction

$$\hat{\rho}_{theo} = \begin{bmatrix} 0.5 & 0 & 0 & 0.5 \\ 0 & 0 & 0 & 0 \\ 0 & 0 & 0 & 0 \\ 0.5 & 0 & 0 & 0.5 \end{bmatrix}$$

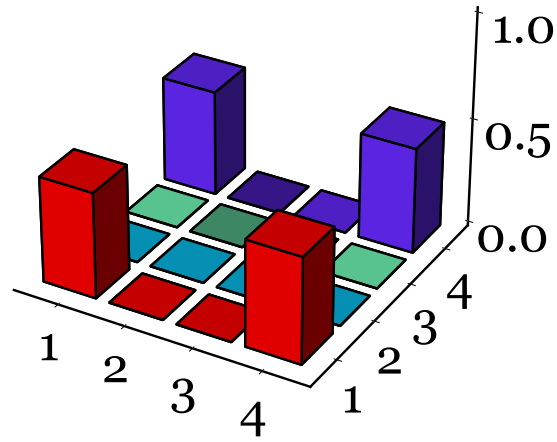
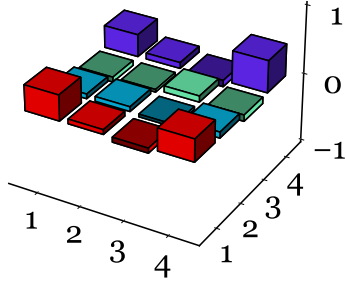


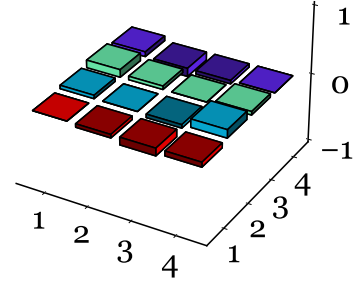
Figure 4.7: Magnitudes of $\hat{\rho}_{theo}$ elements for the $|\Phi^+\rangle$ state.

Experimental results

$$\hat{\rho}_{exp} = \begin{bmatrix} 0.374 & 0.0678 - 0.0498i & -0.0709 - 0.111i & 0.325 - 0.0739i \\ 0.0678 + 0.0498i & 0.0684 & -0.0381 - 0.051i & 0.0857 + 0.12i \\ -0.0709 + 0.111i & -0.0381 + 0.051i & 0.0887 & -0.0921 + 0.0452i \\ 0.325 + 0.0739i & 0.0857 - 0.12i & -0.0921 - 0.0452i & 0.468 \end{bmatrix}$$



(a) Magnitudes of $\Re(\hat{\rho}_{exp})$ elements for the $|\Phi^+\rangle$ state.



(b) Magnitudes of $\Im(\hat{\rho}_{exp})$ elements for the $|\Phi^+\rangle$ state.

Figure 4.8: Magnitudes of $\hat{\rho}_{exp}$ elements for the $|\Phi^+\rangle$ state. Figure 4.8a displays the magnitudes of real elements present in $\hat{\rho}_{exp}$, whereas figure 4.8b displays the magnitudes of imaginary elements present in $\hat{\rho}_{exp}$.

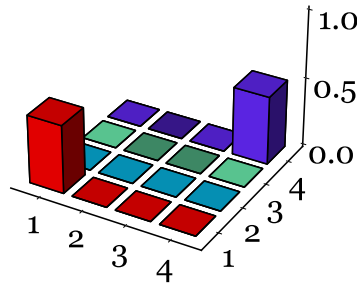
Fidelity	Concurrence	Tangle
0.747	0.655	0.429

Table 4.4: Density matrix characterization quantities calculated for $\hat{\rho}_{exp}$ of $|\Phi^+\rangle$ state.

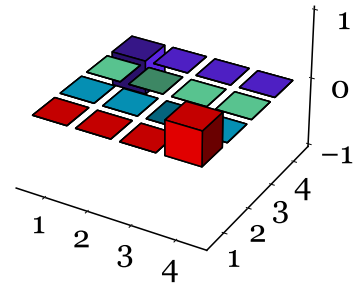
4.2.4 $|\Phi^+\rangle_\phi$ state

Theoretical prediction

$$\hat{\rho}_{theo} = \begin{bmatrix} 0.5 & 0 & 0 & 0.5i \\ 0 & 0 & 0 & 0 \\ 0 & 0 & 0 & 0 \\ -0.5i & 0 & 0 & 0.5 \end{bmatrix}$$



(a) Magnitudes of $\Re(\hat{\rho}_{theo})$ elements for the $|\Phi^+\rangle_\phi$ state.

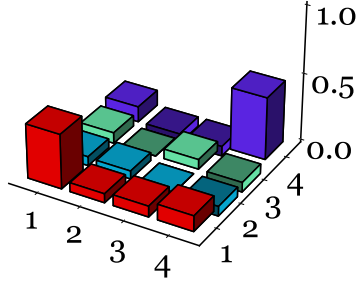


(b) Magnitudes of $\Im(\hat{\rho}_{theo})$ elements for the $|\Phi^+\rangle_\phi$ state.

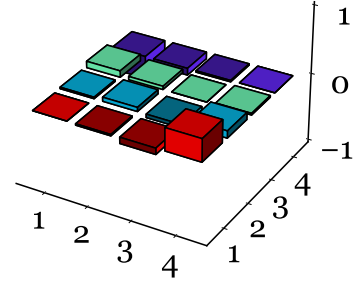
Figure 4.9: Magnitudes of $\hat{\rho}_{theo}$ for the $|\Phi^+\rangle_\phi$ state. Figure 4.9a displays the magnitudes of real elements present in $\hat{\rho}_{theo}$, whereas figure 4.9b displays the magnitudes of imaginary elements present in $\hat{\rho}_{theo}$.

Experimental results

$$\hat{\rho}_{exp} = \begin{bmatrix} 0.404 & 0.0667 - 0.0218i & 0.0796 - 0.0935i & 0.115 + 0.333i \\ 0.0667 + 0.0218i & 0.0593 & 0.00577 - 0.0475i & -0.0714 + 0.103i \\ 0.0796 + 0.0935i & 0.00577 + 0.0475i & 0.072 & -0.0719 + 0.0238i \\ 0.115 - 0.333i & -0.0714 - 0.103i & -0.0719 - 0.0238i & 0.463 \end{bmatrix}$$



(a) Magnitudes of $\Re(\hat{\rho}_{exp})$ elements for the $|\Phi^+\rangle_\phi$ state.



(b) Magnitudes of $\Im(\hat{\rho}_{exp})$ elements for the $|\Phi^+\rangle_\phi$ state.

Figure 4.10: Magnitudes of $\hat{\rho}_{exp}$ elements for the $|\Phi^+\rangle_\phi$ state. Figure 4.10a displays the magnitudes of real elements present in $\hat{\rho}_{exp}$, whereas figure 4.10b displays the magnitudes of imaginary elements present in $\hat{\rho}_{exp}$.

Fidelity	Concurrence	Tangle
0.768	0.671	0.451

Table 4.5: Density matrix characterization quantities calculated for $\hat{\rho}_{exp}$ of $|\Phi^+\rangle_\phi$ state.

Bibliography

- [1] *Spontaneous parametric down-conversion*. C. Couteau. University of Technology of Troyes. 2018.
<https://arxiv.org/ftp/arxiv/papers/1809/1809.00127.pdf>
- [2] *Quantum Mechanics in the Single Photon Laboratory*. M.H. Waseem, F. Illahi & M.S. Anwar. IOP Publishing, July 2020. Online ISBN: 978-0-7503-3063-3, Print ISBN: 978-0-7503-3061-9.
<https://doi.org/10.1088/978-0-7503-3063-3>
- [3] *Some Quantum Optical Experiments with Single Photons and FPGA Programming*. B. Hyder. (LUMS) - Lahore University of Management Sciences. May 2022.
Thesis - Bilal Hyder
- [4] *Experimental test of the violation of local realism in quantum mechanics without bell inequalities*. G. Di Giuseppe, F. De Martini & D. Boschi. Phys. Rev. A, 56:176181, July 1997.
<https://journals.aps.org/prabstract/10.1103/PhysRevA.56.176>
- [5] *Photonic State Tomography*. J.B. Altepeter, E.R. Jeffrey & P.G. Kwiat. Adv. At. Mol. Opt. Phys. 2005.
[https://doi.org/10.1016/S1049-250X\(05\)52003-2](https://doi.org/10.1016/S1049-250X(05)52003-2)